Available online at www.sciencedirect.com
ScienceDirect
Journal of Magnesium and Alloys xxx (xxxx) xxx
www.elsevier.com/locate/jma

Full Length Article

Effects of Ca and Nd addition on plastic instability in extruded Mg-Mn alloy deformed under various conditions

Sang Kyu Woo[a,*], Risheng Pei[b], Talal Al-Samman[b], Dietmar Letzig[a], Sangbong Yi[a,*]

[a] Institute of Materials and Process Design, Helmholtz-Zentrum hereon, 21502 Geesthacht, Germany
[b] Institut für Metallkunde und Materialphysik, RWTH Aachen University, 52056 Aachen, Germany

Received 11 July 2022; received in revised form 15 November 2022; accepted 2 December 2022
Available online xxx

Abstract

Plastic instability, called Portevin-Le-Chatelier (PLC) effect, manifests itself as an unstable plastic flow during tensile tests of structural materials. This phenomenon has a strong influence on diverse properties, leading to unexpected vulnerabilities in the service environment. Among various magnesium-based alloys, PLC phenomenon is most prominently observed in the Mg-Mn-Nd alloy under elevated temperature and low strain rate conditions. An important aim of the study is to clarify and compare the significance of the RE and Ca addition, which are known to cause a formation of a largely weakened non-basal type texture, in the occurrence of plastic instability. Due to the PLC phenomenon, there is a risk of weakening texture and formability improvement by the addition of RE and Ca elements in Mg alloys. Based on the understanding of the role of Nd to the PLC phenomenon in Mg-Mn alloy identified in previous studies, the PLC characteristics according to alloying elements and deformation conditions were compared and analyzed. To identify the micromechanical mechanisms of the PLC phenomenon, varies in the microstructure and mechanical properties during deformation of Mg-Mn binary and Ca or Nd-containing Mg-Mn-based ternary alloys in various conditions were systemically analyzed. The addition of Ca did not show a marked PLC effect due to the formation of low number density Mn-Ca and Ca-Ca solute clusters and an unbalanced Mn:Ca ratio. In contrast, the addition of Nd leads to the formation of a higher number density of Nd-Nd and Mn-Nd solute clusters than that of Ca-Ca and Mn-Ca solute clusters of the Mg-Mn-Ca alloy, resulting in a stable solute-dislocation interaction atmosphere under specific ranges of deformation temperature and strain rate. The deformation in the regime of PLC phenomenon, results in a decrease in ductility and an increase in strength, despite deformation at elevated temperatures with maintaining the weakened texture.

Keywords: Magnesium; Plastic instability; Portevin–Le Chatelier effect; Solute cluster; Neodymium; Calcium.

1. Introduction

Plastic instability, commonly known as the Portevin–Le Chatelier (PLC) effect, occurs in the form of heterogeneous behavior called ‘serration flow’ or ‘jerky flow’ and is known to be observed under specific ranges of strain rate and temperature in certain alloys during mechanical tests [1–3]. The PLC effect has a strong influence on diverse materials’ properties. It increases flow stress, ultimate tensile strength, and the work hardening rate, while the ductility suffers from a corresponding decrease in the strain rate sensitivity coefficient and fracture toughness [1]. It causes unexpected vulnerabilities in the service environment of the materials. The occurrence of PLC phenomenon, serrations or discontinuous yielding on a stress-strain curve is commonly observed in macroscopic manifestations of the dynamic strain aging (DSA) phenomenon associated with the negative strain rate sensitivity (nSRS). Thus, the main mechanism for PLC effect could be ascribed to the DSA, i.e. the interaction between solute atoms, precipitates and mobile dislocations [1–3]. This phenomenon has been extensively researched in order to understand the underlying microscopic mechanisms in various materials such as steels,

* Co-corresponding authors.
E-mail addresses: sangkyu.woo@hereon.de (S.K. Woo), sangbong.yi@hereon.de (S. Yi).

https://doi.org/10.1016/j.jma.2022.12.004

Please cite this article as: S.K. Woo, R. Pei, T. Al-Samman et al., Effects of Ca and Nd addition on plastic instability in extruded Mg-Mn alloy deformed under various conditions, Journal of Magnesium and Alloys, https://doi.org/10.1016/j.jma.2022.12.004

Cu and Al alloys. The research scope has been extended to Mg alloys, and related studies on various alloy systems such as Mg-Al-based [4–7], Mg-Zn-based [8–10], Mg-RE-based [7,8, 11–13], Mg-Li-based [3,14–17], Mg-Ca-based [18], and Mg-Ag-based [19] are continuing. However, the mechanism is not yet clearly identified, and this phenomenon is controlled by more complicated and various factors depending on the alloying elements.

For decades, many researches have been conducted to improve the room temperature (RT) formability of Mg alloys. Until recently, it has been widely accepted that the addition of alloying elements of RE and/or Ca to Mg forms a significantly weaker texture during thermo-mechanical treatments, in comparison to the commercial AZ-based alloys [20–25]. The weak texture with a more randomized distribution of the crystallographic basal plan (0001) of the Mg alloy due to the addition of RE or Ca allows the accelerated dislocation slip on the basal plane, the main deformation mechanism of Mg alloys. This leads to an improved RT ductility, reduced tensile and compressive anisotropy, balanced strain hardening, and excellent sheet formability. According to several studies [26–29], Mg alloys containing Mn and RE elements tend to form a weak texture after extrusion. These weakly textured extruded profiles show a high ductility as well as small or disappearing asymmetry in tensile and compressive yield strength. In addition to the texture weakening, the addition of RE and Ca affects the activation of various deformation mechanisms of the Mg alloy, so studies on this have been actively conducted in various fields. Nevertheless, the PLC phenomenon may significantly deteriorate the properties of the Mg alloys or cause unexpected premature fractures under service conditions.

In a previous study [29], the microstructure, texture, and mechanical behavior of extruded Mg-Mn binary alloy (i.e. M1) and Mg-Mn-Nd ternary alloy (i.e. MN11) were evaluated and the correlation between the development of texture and occurrence of the PLC phenomenon was closely analyzed. According to this study, the addition of Nd significantly contributes to the grain refinement and the randomization and weakening of texture. Nevertheless, a dramatic decrease in elongation was caused even at high-temperature deformation with severe PLC phenomenon during deformation under elevated temperature and low strain rate conditions. Related to this, under the condition of PLC prominent, the initial RE texture was maintained even after deformation, and lattice rotation was suppressed. Subsequent studies focused on the correlation between the PLC mechanism and the microstructure of MN11 alloy [30]. The microstructure and PLC properties of as-extruded MN11 alloy (i.e. MN11-AE) and heat-treated at 275 °C for 120 min. (i.e. MN11-HT) specimens were compared, and the research to investigate the correlation between the tendency of solute clustering and solute-dislocation interaction was carried out. Under the same deformation conditions, the PLC phenomenon in the MN11-AE specimen was significantly weakened in the MN11-HT specimen, which is due to the microstructural change. After the annealing process, a large number of fine particles were precipitated and the concentration of the solute was reduced in MN11 alloy, which caused changes in the ratio and number density of the solute cluster. This inhibited the formation of a stable Cottrell-Bilby cloud atmosphere, disrupted the solute-dislocation interaction, and consequently resulted in the weakening of the PLC effect.

Table 1
Chemical composition of Mg-Mn-based alloys measured by spark OES [29].

Alloy	Mg	Mn	Ca	Nd	Si	Fe
		wt.%			wt.ppm	
M1		0.98	–	–	18	72
MX10	Bal.	1.01	0.27	–	37	85
MN11		0.98	–	1.13	24	109

In previous studies, the correlation between changes in microstructure and texture and the occurrence of PLC phenomenon when Nd was added to Mg-Mn alloys was investigated, and a solute-dislocation interaction mechanism was proposed based on solute clustering. In this study, by benchmarking previous studies, an extended study was performed to identify factors affecting the PLC phenomenon. From that point of view, the correlation between the addition of Ca, which is another element to contribute to the weakening of the texture of the extruded Mg-Mn, and the PLC properties was focused on. The aim of this study is to unravel the micro-mechanical mechanism of the PLC effect in the binary extruded Mg-Mn alloy and newly developed extruded Mg-Mn-Ca and Mg-Mn-Nd alloys under various temperatures and strain rates. After defining the deformation conditions in which the PLC effect is evident, the correlation between the mechanical deformation behavior and the microstructural difference is analyzed in detail. Based on this, insights are obtained into possible mechanisms that can trigger or suppress plastic instability in conjunction with the alloy chemistry and deformation conditions.

2. Experimental procedure

Pure Mg ingot and Mg-Mn, Mg-Ca, and Mg-Nd master alloys were used for casting. The alloys with the nominal compositions of M1 (Mg-1 wt.%Mn), MX10 (Mg-1 wt.%Mn-0.3 wt.%Ca), and MN11 (Mg-1 wt.%Mn-1 wt.%Nd) were molten in a crucible under a protective gas atmosphere. The melt was poured into a cylindrical steel mold and quenched with the mold in water. Table 1 shows the chemical composition of M1, MX10, and MN11 alloys measured by spark optical emission spectroscopy (OES). The cast billets were machined to 49 mm in diameter for extrusion and were homogenized for 16 h at 450 °C before extrusion. The billets were preheated to 300 °C and then directly extruded to a round bar with 8 mm in diameter, corresponding to the extrusion ratio of 37.5:1 and ram speed of 2.5 mm/*sec*.

Microstructural characterization of the extruded bars was conducted using an optical microscope (OM, Nikon Optiphot 200) and a dual-beam scanning electron microscope (Zeiss, Crossbeam 550) equipped with a focused ion beam (FIB),

integrated energy dispersive x-ray spectroscopy (EDX), and scanning transmission electron microscopy (STEM) detectors. For microscopy, the mounted specimens in epoxy resin were mechanically ground using SiC papers up to #2400 grit and then polished using 3 μm diamond paste and water-free oxide polishing suspension. The polished specimens were etched using a mixed solution of 1 mL of nitric acid, 20 mL of distilled water, 20 mL of acetic acid, and 70 mL of ethylene glycol. For high-resolution observations, the specimens were collected from the region of interest using FIB milling after conventional mechanical grinding and polishing, and observed using STEM detector at an acceleration voltage of 30 kV.

The mechanical properties of the extruded alloys were examined using round specimens with a gage length of 20 mm and a diameter of 4 mm. Tensile tests were carried out using a universal testing machine (Zwick, Z050) equipped with a heating furnace at various temperatures (RT, 100, 150, 200, and 250 °C) and strain rates (10^{-2} /s, 10^{-3} /s, and 10^{-4} /s) in the extrusion direction. Prior to the mechanical loading, the specimens were preheated at the testing temperature for 10 min to ensure temperature uniformity over the specimen. After the tensile test, the specimens were immediately quenched in a water bath at RT in order to avoid the microstructure change due to slow cooling. Furthermore, strain rate jump tests were carried out to determine the SRS, m-value. The strain rates were increased in 5 steps from 10^{-4} to 10^{-2} /s at each testing temperature.

Elemental distributions of Mn, Ca, and Nd in connection with precipitates and grain boundaries in as-extruded M1, MX10, and MN11 alloys were characterized by atom probe tomography (APT) using a Local Electrode Atom Probe 4000X HR from Cameca. Laser-pulsing mode with an ultraviolet laser (wavelength 355 nm) was selected to ensure stable measurements with a pulse energy of 30 pJ and frequency of 125 kHz. The temperature during the measurement was set to 30 K. APT specimens were prepared by focused ion beam milling at 30 kV and cleaning at 2 kV. The tips were then reconstructed by the commercial IVAS 3.8.0 software package from Cameca. To trace the position of grain boundaries and guide tips milling, transmission Kikuchi diffraction-EBSD (TKD-EBSD) was performed on the same tip at 30 kV and 5.5 nA.

3. Results

Fig. 1 shows the optical micrographs of the investigated extruded alloys (M1, MX10, and MN11). The M1 alloy shows an inhomogeneous grain size distribution, and the average grain size is classified into two groups: a relatively fine grain group of 14.9 ± 1.1 μm and a relatively large grain group of 36.2 ± 1.0 μm. However, the grains were refined by the addition of Ca and Nd. The MX10 alloy has a uniform and smaller average grain size of 13.9 ± 1.0 μm than M1 alloy. A finer grain structure was observed in the MN11 alloy with an average grain size of 8.8 ± 1.0 μm, in comparison to the M1 and MX10 alloys.

The SEM backscatter electron (BSE) images show a clear contrast of precipitates to the matrix, Fig. 2, and the insets are the magnified images near the grain boundaries observed by STEM. The statistical assessment of the observed precipitates and their size distribution of each alloy were calculated from 50 BSE images with an area of 517.5 × 27.6 μm^2 and plotted in Fig. 2(d). As shown in Fig. 2, very small particles with the size of 150–250 nm were observed in all alloys. The M1 and MX10 alloys show a similar quantitative characteristic of precipitates, and most of them were identified as Mn-containing phases via SEM-EDX measurements. Some Ca-containing phases were detected, but the Mg-Mn-Ca ternary phase was not identified in the MX10 alloy. The MN11 alloy has a large amount (high number density) of finer precipitates (smaller area and area fraction). Fine Nd-containing phases were detected along with grain boundaries and grain interior, and some Mn-containing phases were also detected in the grains.

Macro tensile tests were carried out under various temperature and strain rate conditions for each alloy.

Fig. 3(a), (b), (c), (d), and (e) show the tensile stress-strain curves of the examined alloys at different strain rates (10^{-2} /s, 10^{-3} /s, and 10^{-4} /s) and temperatures (RT, 100 °C, 150 °C, 200 °C, 250 °C). The M1 and MX10 alloys depicted typical flow behavior characterized by a decrease in strength and an increase in elongation by increasing the deformation temperature and decreasing the strain rate. Regarding serrated flow, both alloys showed negligible serrations in the stress-strain curves at high temperatures and low strain rates. A distinct behavior was observed in the MN11 alloy, with severe serrations at 10^{-3} /s and 10^{-4} /s and temperatures above 150 °C. As shown in Fig. 3(a), the relatively weak serration at RT became larger at 150 °C and 10^{-4} /s to reach a stress amplitude of almost 10 MPa, Fig. 3(c). These serrations tended to stand out as the temperature increased and the strain rate lowered. It is noteworthy that this severe serration diminished again at higher temperatures, i.e. 250 °C, Fig. 3(e). The serration flow is considered to be typical of unstable plastic flow during the tensile loading of structural materials due to the plastic instability. As shown in Fig. 3, it is well known that it appears prominently in certain alloys, under certain temperature and strain conditions [1–3].

Fig. 4(a), (b), and (c) provide a quantitative analysis of the degree of serrations in the flow curves of the M1, MX10, and MN11 alloys for various deformation conditions, respectively. In the case of M1 and MX10 alloys, the serrations became more visible at elevated temperatures and low strain rates, corresponding to Fig. 3. In practice, the serrations in the MX10 alloy are slightly more severe than in the M1 alloy, but the difference is not pronounced as shown in Fig. 4. The max stress amplitudes, i.e. serration, of these alloys are $1 \leq \Delta\sigma \leq 5$ MPa at low strain rates and high temperatures. By comparison, severe serrations were observed during the deformation of the MN11 alloy at 150 °C and 10^{-4} /s with the stress amplitude of $\Delta\sigma \geq 10$ MPa, which decreases at 250 °C. The severe serrations and distinctive temperature and strain rate-dependent trends in the MN11 alloy are well pre-

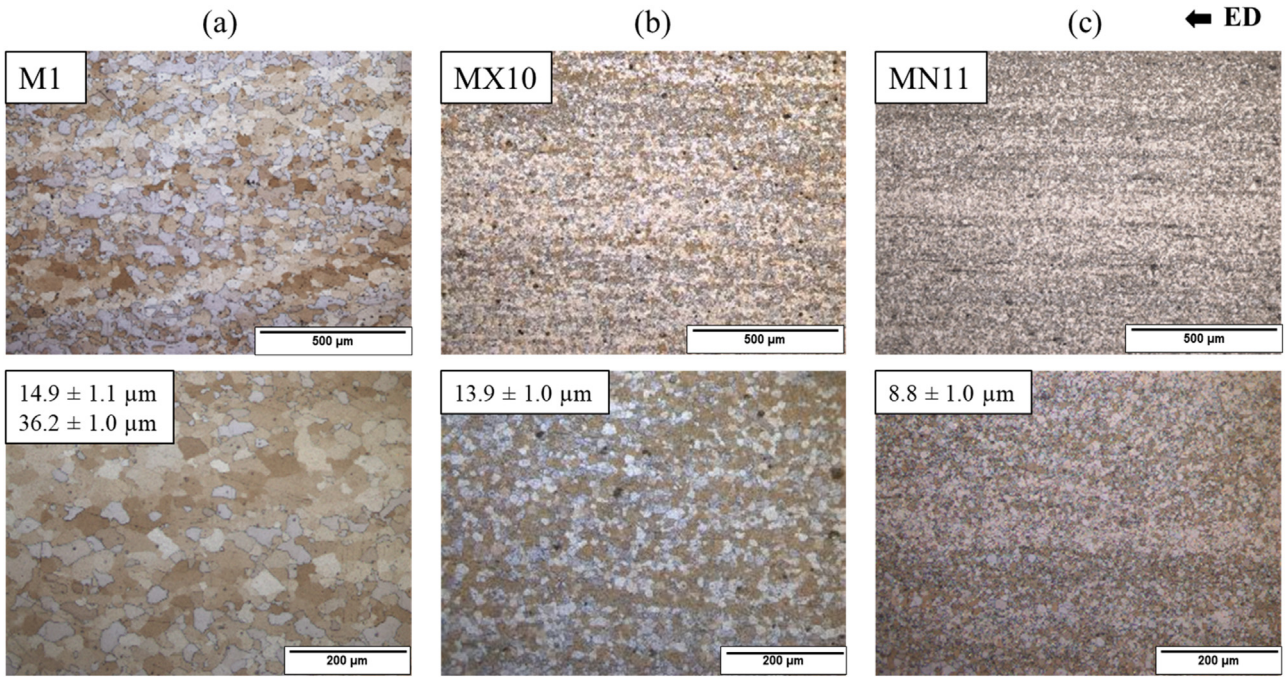

Fig. 1. Microstructure of extruded (a) M1, (b) MX10, and (c) MN11 alloys observed using an optical microscope [29].

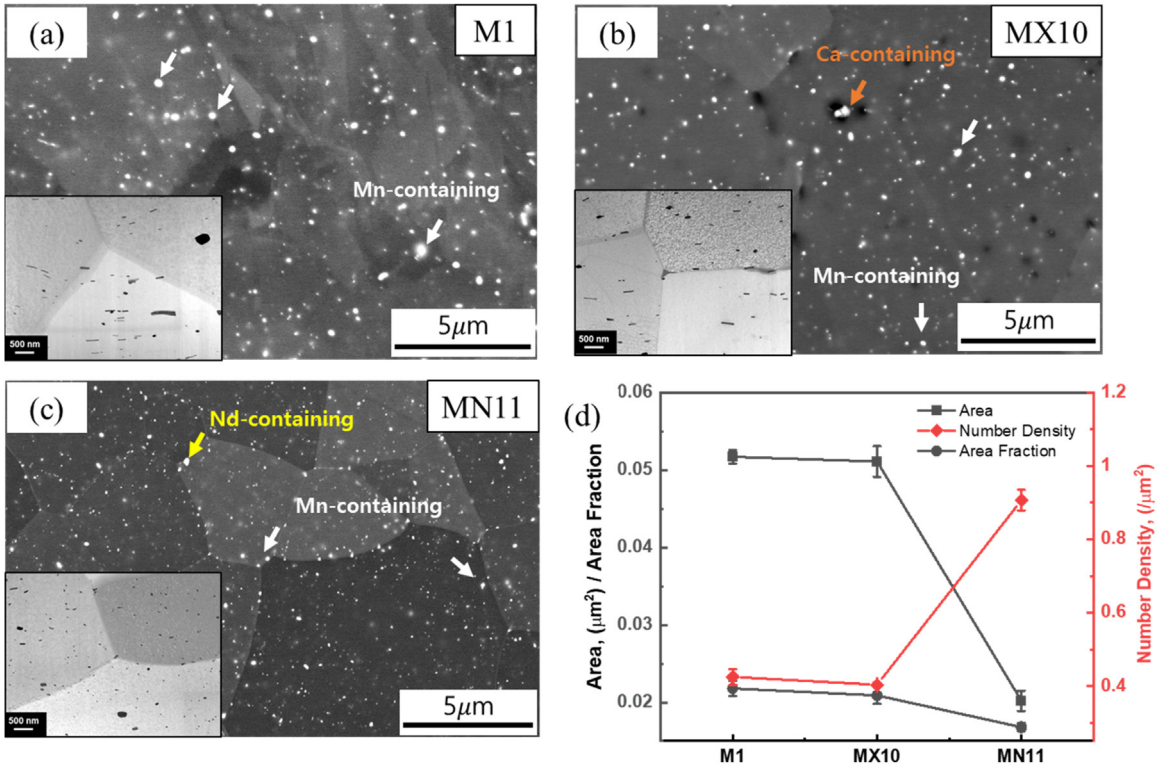

Fig. 2. SEM-BSE images of (a) M1, (b) MX10, and (c) MN11 [30] alloys, (d) quantitative analysis of precipitates found in M1, MX1 and MN11 alloys presented in terms average area, average area fraction as well as number density.

sented in Fig. 4(c). It is noteworthy that the type of serrations detected at 10^{-3} /s and 10^{-4} /s was not the same. The serration behaviors at 10^{-3} /s and 10^{-4} /s are classified into different types, their characteristics seemed to correspond to what is known as types A, B, and C serrations [1,31–33]. The 'type A' band mainly occurs at high strains and has relatively small amplitudes, but periodically large amplitudes are observed in the long term. The 'type B' band occurs mainly at medium strains and has a characteristic large amplitude accompanied by a stress drop in a very short period of time.

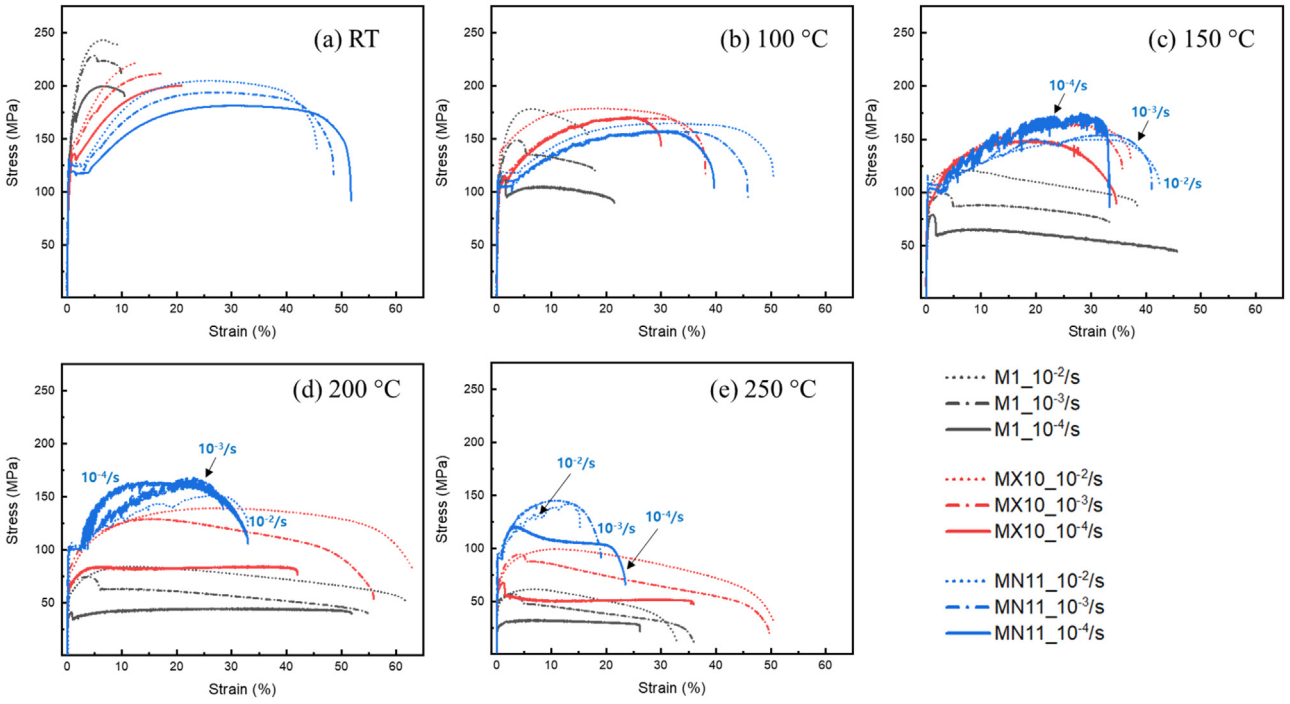

Fig. 3. Macro Tensile stress-strain curves obtained at different temperatures and strain rates for M1, MX10, and MN11 alloys; (a) RT, (b) 100 °C, (c) 150 °C, (d) 200 °C, and (e) 250 °C.

Creates an overlapping serration in addition to the typical serrations of type A. This pattern is observed periodically over a long period of time. The 'type C' bands occur mainly at very low strain rates, resulting in large amplitude stress drops and forming pseudo-periodic patterns with large periods. The stress-strain curve is heavily serrated in this case. Sometimes these types are observed overlapping or alternating. The serration at 10^{-3} /s corresponds to type A, while a mixed type of serration similar to type B is observed at the strain rate of 10^{-4} /s [29, 30]. Fig. 4(d) presents the estimated SRS, m, at different temperatures. The SRS parameter 'm' is expressed as Eq. (1.1), where $\sigma 1$ and $\sigma 2$ are the flow stresses at each strain rates $\dot{\varepsilon}1$ and $\dot{\varepsilon}2$, and 'n' is the strain sensitivity coefficient [29,34,35].

$$m = \frac{\partial ln\sigma}{\partial ln\ \dot{\varepsilon}} \cong \frac{\ln\left(\frac{\sigma 2}{\sigma 1}\right)}{\ln\left(\frac{\dot{\varepsilon}2}{\dot{\varepsilon}1}\right)} = \frac{1}{n} \tag{1.1}$$

The m-values of MN11 alloy were demonstrated negative m-values, i.e. nSRS, at lower strain rates (between 10^{-4} /s and 10^{-3} /s) and the elevated temperatures (between 100 and 200 °C). The nSRS is well-known as a macroscopic indication of DSA [35,36]. The DSA is observed in association with an increase in strength and a decrease in fracture elongation of the MN11 alloy under conditions where strong serration is observed (cf. Fig. 3). Fig. 5(a), (b), and (c) show varies in yield strength (YS), ultimate tensile strength (UTS), and elongation (El.) with temperatures of M1, MX10, and MN11 alloys, respectively. In general, an increase in temperature is accompanied by a decrease in strength and an increase in elongation. As shown in Fig. 5(a) and (b), M1 and MX10 alloys follow these general trends. On the other hand, the MN11 alloy does not follow and depart from this trend. Despite the increase in temperature, the strength increased in the specific temperature range and the elongation was rather decreased. This unusual trend is based on the PLC phenomenon related to characteristics of DSA, which is observed with strong serration in Figs. 3 and 4. Similarly, the slower reduction of the strength and the decrease of elongation at 250 °C of the M1 and MX10 alloys were accompanied with the occurrence of serration at elevated temperatures. It is to mention that the MN11 alloy had a reduced degree of serration at 250 °C, different from the M1 and MX10 alloys showing the prominent PLC characteristics. This trend is more clearly observed in the M1 alloy than in the MX10 alloy. Nevertheless, the degree of serration in M1 and MX10 alloys is still not comparable to that of MN11 alloy. The above results show the obvious PLC phenomenon observed in MN11 alloy, especially at low strain rates and elevated temperatures. It also shows that there are differences in the conditions and behaviors under which the PLC phenomenon is observed depending on the alloying elements. As mentioned earlier, the main mechanism for the PLC effect could be ascribed to the interaction between solute atoms and mobile dislocations [1–3]. Therefore, understanding the difference in type and distribution of solutes according to alloying elements is an essential process in identifying the mechanism for the difference in the PLC phenomenon of each alloy.

The solute behaviors, such as segregation to grain boundaries (GBs), precipitation, and solute clustering were examined closely using 3D APT. Fig. 6 shows reconstructed APT tips from M1, MX10, and MN11 alloys. In the M1 alloy, Mn segregation along the sampled boundary segment revealed a

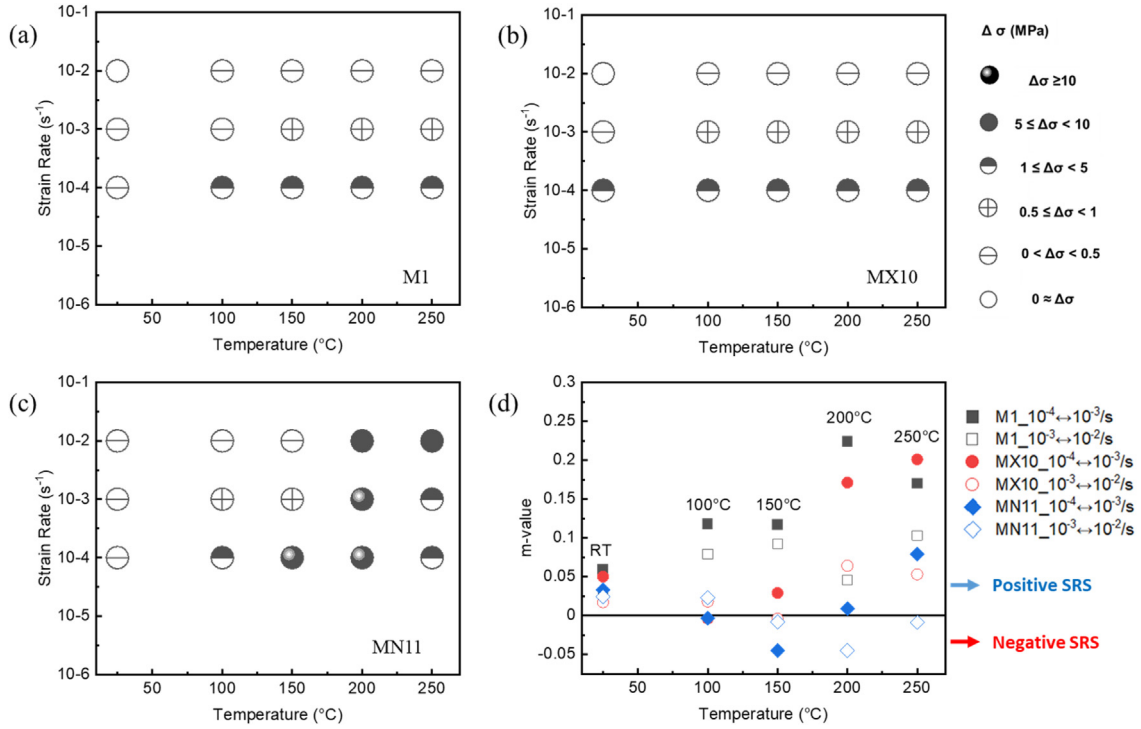

Fig. 4. Quantitative analysis of the degree of flow serrations in the stress-strain curves in Fig. 3 for (a) M1, (b) MX10, and (c) MN11 alloys. The stress amplitude $\Delta\sigma$ indicates the difference in stress between the highest and lowest serration points. (d) Calculated strain rate sensitivity, m, for all alloys at different deformation conditions.

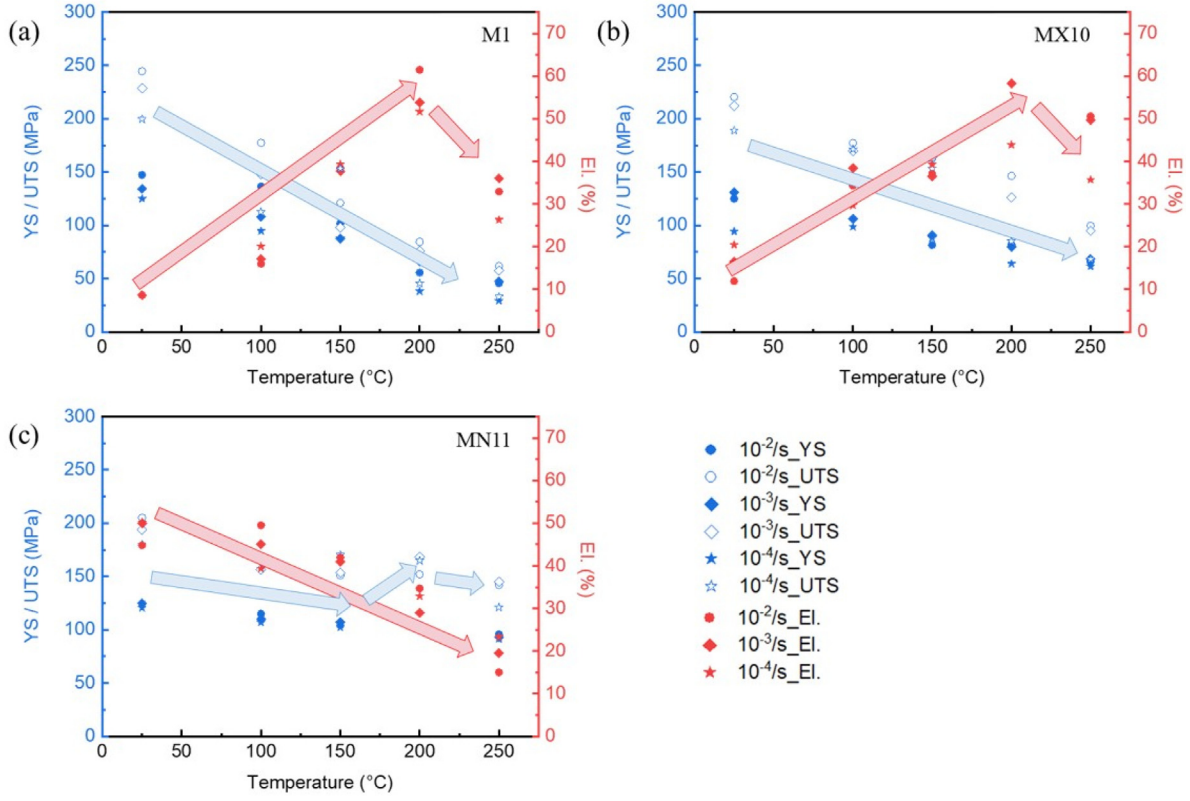

Fig. 5. Yield strength (YS), ultimate tensile strength (UTS), and elongation (El.) obtained at different temperatures and strain rates in the stress-strain curves in Fig. 3 for (a) M1, (b) MX10, and (c) MN11 alloys. Arrows show the trend of each value of YS, UTS (blue) and El. (red) with temperature.

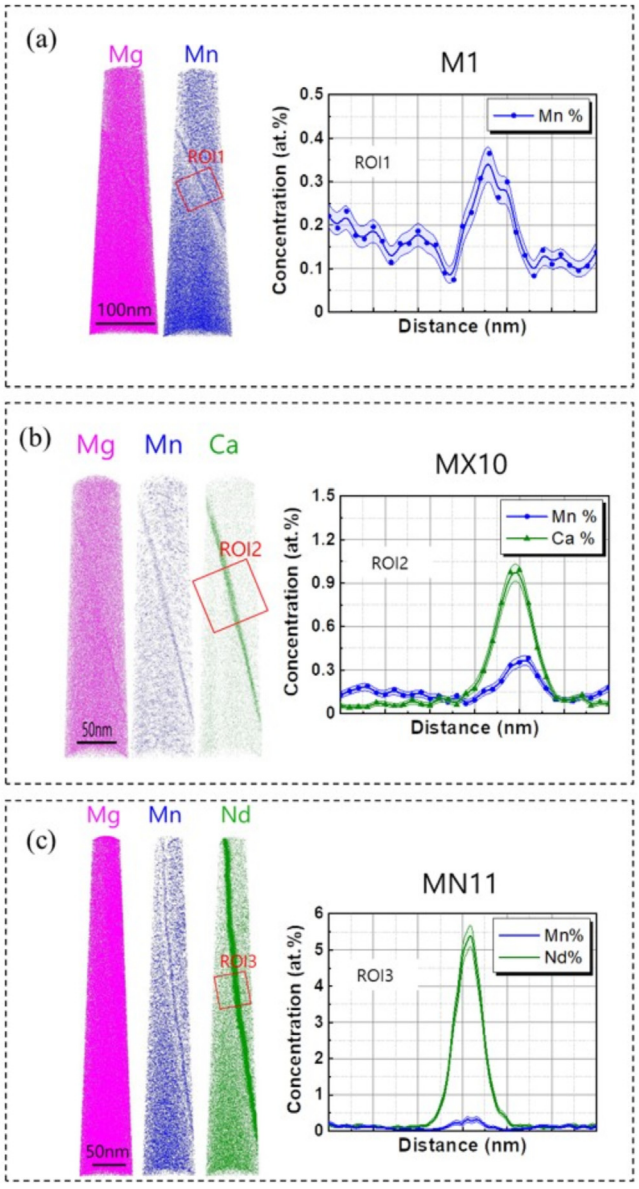

Fig. 6. Reconstructed 3D APT tips of (a) M1, (b) MX10, and (c) MN11 [30] alloys with grain boundaries showing elemental distributions of Mg, Mn, Ca, and Nd along with solute concentration profiles within the respective cylindrical regions of interest (ROIs).

peak concentration of 0.35 at.%, Fig. 6(a). The bulk concentration of Mn varied in comparison between 0.1 and 0.2 at.%, which was less than the nominal alloy concentration of 0.44 at.%. It is considered that the composition of the matrix and segregation region is lower than the nominal composition due to the formation of the secondary phase. The addition of another solute, as in the MX10 alloy, demonstrated co-segregation of Mn and Ca to the GB with peak concentrations around 0.35 at.% and 1.0 at.%, respectively, Fig. 6(b). The latter is almost 17 times higher than the bulk concentration of 0.06 at.%. For the MN11 alloy, the concentration profiles measured within the cylindrical region of interest in the MN11 alloy revealed a strong GB segregation tendency of Nd attaining concentration levels of 25 times higher than the bulk concentration (5.6 at.% vs. 0.25 at.%), Fig. 6(c).

Solute atom cluster analysis based on APT data mining [37,38] of the measured tips in Fig. 6 was employed to examine the types of solute clusters and assess their interaction efficiency with matrix dislocations and site-specific segregation to microstructural defects. The first order of nearest neighbor (1NN) distribution of Mn, Ca, and Nd atoms was used in the analysis. The point of maximum difference between the experimental and random 1NN distributions was chosen as $d_{max} = 2$ nm. Different minimum atom numbers (N_{min}) were tested to identify and isolate the clusters and N_{min} was determined at the maximum value, where the experimental 1NN distribution of Mn, Ca, and Nd in the resulting matrix was nearly identical to the random one ($N_{min} = 4$ atoms). Atoms in clusters of less than N_{min} are considered matrix atoms. The parameters of envelope distance and erosion diameter were both set to 0.5 d_{max} (1 nm) [30]. The statistical results of the cluster analysis are listed in Table 2. In the M1 alloy, a high density (approximately 1089 $\times 10^{15}$ cm^{-3}) of small Mn-Mn clusters with 4-6 atoms was detected. With the addition of further solute, i.e. Ca and Nd in the MX10 and MN11 alloys, the density of such Mn-Mn clusters decreased significantly, because Mn atoms were also evident in binary Mn-Ca and Mn-Nd clusters. The density of Mn-Ca and Mn-Nd clusters with a size of 4-6 atoms were approximately 637 $\times 10^{15}$ cm^{-3} and 914 $\times 10^{15}$ cm^{-3}, respectively. The number densities in most of the cluster sizes considered were higher in the MN11 in comparison to the MX10 specimen. For example, the number density of small clusters consisting of 4-6 atoms and 7-10 atoms in the MN11 specimen was 43% and 48% higher than in the MX10 specimen, respectively. The number density of the mid-size (11 – 25 atoms) clusters was similar, while the MN11 specimen showed a higher density of the large clusters (> 30 atoms) than in the MX10 specimen. In the MX10 specimen, more Mn-Mn clusters were found than in the MN11 specimen. With respect to Ca-Ca and Nd-Nd clusters, the number densities of these clusters were much larger in the MN11 specimen than that in the counterpart MX10 specimen, 97×10^{15} cm^{-3} and 31×10^{15} cm^{-3}). Interestingly, the number density of Ca-Ca and Nd-Nd clusters was comparatively lower than the Mn-Ca and Mn-Nd clusters, suggesting that the formation of co-clusters in these alloys is more favorable than in single-species clusters.

4. Discussion

Figs. 3-5 show the results that the PLC properties of the three types of Mg-Mn-based alloys depend on the alloying elements, temperatures, and strain rates. The PLC phenomenon expressed in the form of serration in the strain-stress curves was clearly marked by the addition of Nd, unlike in the Mg-Mn binary alloy (cf. Figs. 3 and 4), while the Ca addition had a smaller effect in comparison to the Nd addition. The serration was more severe as the temperature increased and the strain rate decreased in the same alloys. In the case of MN11 alloy, it showed a clear nSRS under the condition between

Table 2
Compositions (at.%) and number density ($\times 10^{15}$ cm^{-3}) of different solute atom clusters in the matrix in M1, MX10, and MN11 [30] alloys.

M1			MX10			MN11		
Cluster type	Cluster size	Number density ($\times 10^{15}$ cm^{-3})	Cluster type	Cluster size	Number density ($\times 10^{15}$ cm^{-3})	Cluster type	Cluster size	Number density ($\times 10^{15}$ cm^{-3})
Mn-Mn	4–6	1089.11	**Mn–Mn**	4–6	210.05	**Mn–Mn**	4–6	61.53
	7–10	507.06						
	11–15	257.89		7–10	84.89		7–10	7.84
	16–30	192.03		>10	28.29		>10	0
	>30	44.04						
			Ca-Ca	4–8	31.56	**Nd-Nd**	4–9	97.73
			Mn-Ca	4–6	637.78	**Mn–Nd**	4–6	914.60
				7–10	330.86		7–10	488.67
				11–15	230.73		11–15	235.28
				16–20	114.27		16–20	101.35
				21–30	68.56		21–25	54.90
				>30	93.59		>25	120.66
				Mn (at.%)	70.37		Mn (at.%)	50.27
				Ca (at.%)	29.62		Nd (at.%)	49.72

100 °C and 200 °C, Fig. 4(d), which shows that the PLC phenomenon clearly occurred under these conditions. MN11 alloy showed severe serration up to 200 °C, but it was clearly decreased at 250 °C. It is obviously different from the trend in M1 and MX10 alloys which the PLC phenomenon is maintained even at 250 °C, as shown in Fig. 4 (a-c). It is believed that the occurrence and the different tendency of the PLC phenomenon distinguished in the MN11 alloy are due to the change in the mechanism of the PLC phenomenon according to the addition of Nd. Several studies have reported the occurrence and possible mechanisms of the PLC phenomenon according to Nd-containing alloys such as Mg-Mn-Nd [29,30], Mg-Zn-Nd [10,33], and Mg-Y-Nd [39], and researchers have suggested several possible mechanisms.

According to the Cottrell-Bilby theory [40], the appearance of the upper yield point in the stress-strain curve is attributed to dislocation pinning by interstitial solute atoms. A similar principle can be extended to substitutional alloys given that bulky solute atoms such as Nd tend to gather under dislocations forming a Cottrell-atmosphere that restricts dislocation motion [30]. The influence of Cottrell-Bilby clouds on macroscopic deformation behavior was not only limited to yielding and the Lüders band generation but was also responsible for DSA and PLC behavior during deformation at elevated temperatures. In a previous study on the PLC phenomenon of Mg-Mn-Nd alloy [30], the possibility of Mn-Nd and Nd-Nd clusters to form stable Cottrell-Bilby clouds, which can effectively fix dislocation movement, was shown. The region where DSA occurs is highly dependent on the deformation temperature and strain rate, as it controls the diffusivity of solute atoms and movement velocity of dislocation. Therefore, the absence of a serrated stress-strain response at RT may be due to the difficulty of pinning-unpinning cycles because the solute cloud cannot diffuse into dislocations at low temperatures [30]. At low temperatures, the solute does not diffuse well enough to fix the movement of the dislocation. Conversely, at high strain rates, a similar situation can occur when the limitation of dislocation movement is exceeded. Movement of dislocation that exceeds the diffusion rate of the solute makes it difficult to form a fixed atmosphere. This is closely related to severe serration only at certain temperatures and strain rates. The difference in the tendency of the PLC phenomenon according to temperature and strain rate in the MN11 alloy had a dominant effect on mechanical properties, Fig. 5. The gradual decrease and increase at a certain temperature range in stress and decrease in elongation with increasing temperature in MN11 alloy is significant evidence for the occurrence of PLC. The M1 and MX10 alloys show a similar tendency of stress and elongation compared to the MN11 alloy at elevated temperatures, which is due to the occurrence of the PLC phenomenon at elevated temperatures in these two alloys.

From the solute cluster analysis in Table 2, some clues are provided as to the reasons that the addition of Ca does not cause the prominent PLC phenomenon as much as the addition of Nd does in Mg-Mn alloy. The Ca-Ca cluster and Mn-Ca cluster in the MX10 alloy, Table 2, have lower number densities than those of the Nd-Nd and Mn-Nd clusters in the MN11 alloy while the former has a higher number density of Mn-Mn clusters. Such differences in the cluster density between MN11 and MX10 alloys are comparable to those between MN11 alloy AE (as-extruded) and HT (heat-treated at 275 °C for 2 h), as shown in previous studies [30]. The low cluster density in the MN11-HT specimen is attributed to the depletion of the Nd solute due to the formation of Mg_3Nd precipitates by heat treatment. The depletion of Nd solutes suppresses the formation of a sufficient amount of Nd-Nd and Mn-Nd clusters and significantly reduced the pinning effect on the dislocations. In other words, the addition of Ca is considered to be a difficult condition to form a cluster that can form a stable Cottrell-Bilby cloud which effectively fixes the dislocation movement compared to the addition of Nd. In this study, most of the Ca added in the MX10 alloy was consumed to form the coarse Mg-Ca phase (cf. Fig. 2),

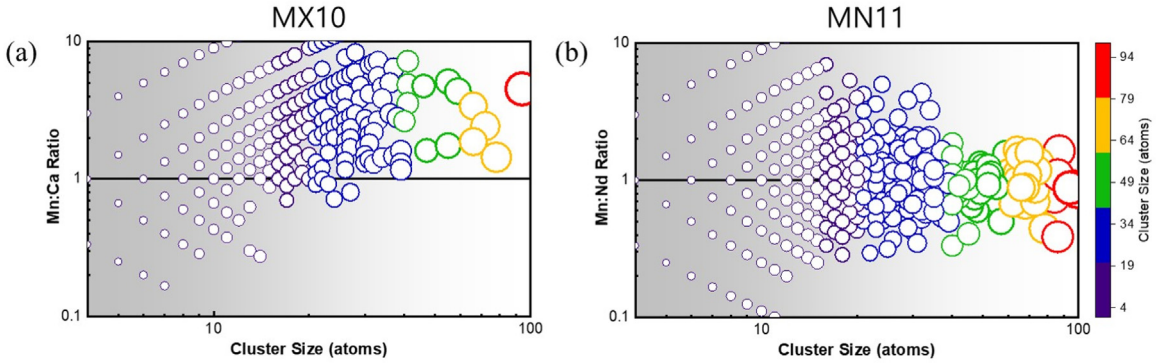

Fig. 7. Cluster analysis of atoms in the MX10 and MN11 alloy specimens. (a) Mn-Ca and (b) Mn-Nd [30] clusters concentration in terms of Mn:Ca and Mn:Nd ratio as a function of cluster size, respectively (The size of the circle symbol is proportional to the size of the cluster).

and the concentration of solute in the matrix was measured to be relatively low compared to that of the MN11 alloy as presented in Fig. 6 (0.06 Ca vs. 0.25 Nd at.%). It is considered that the depletion of Ca solute in the matrix of MX10 alloy caused a decrease in the number density of clusters similar to the case of the MN11-HT specimen.

Furthermore, it is also worth paying attention to the different ratios of Ca and Nd to Mn in the Mn-Ca and Mn-Nd solute clusters, respectively. In the MN11 specimen, the average composition of the Mn-Nd clusters was almost 50% Nd and 50% Mn. However, in the MX10 specimen, the Mn:Ca ratio was approximately 7:3. (cf. Table 2) The relationship between cluster size and composition is shown in Fig. 7 for both MX10 and MN11 specimens. Interestingly, for clusters with a size smaller than 10, the ratio between Mn:Ca is random, whereas when the Mn-Ca cluster is larger than 10 atoms, the Mn:Ca ratio becomes higher than 1 and in some cases reaches 10. This indicates that large clusters are formed by absorbing adjacent Mn atoms. The ratio of Mn:Ca is about 7:3, which is similar to the ratio of the MN11-HT specimen [30], and is clearly distinct from the ratio of Mn:Nd, which has a ratio close to 1.

On the other hand, the number density of Ca-Ca and Nd-Nd clusters was much lower than that of Mn-Ca and Mn-Nd clusters, suggesting that the formation of co-clusters in these alloys is more favorable than in single-clusters. For the small clusters (<10 atoms) in the MX10 and MN11 specimens, no preference for the Mn:Ca and Mn:Nd concentrations was found, indicating also that Mn and Ca, Nd atoms tend to co-cluster favorably. Thus, it is possible to pay attention to the role of the cluster including Mn. Co-clusters may form more favorably and stably compare to Mn-Mn, Ca-Ca, and Nd-Nd single clusters, contributing to the formation of stable Cottrell-Bilby clouds, which is considered to be highly correlated with the development of the PLC phenomenon in Mn-containing alloys.

The difference in the formation of solute clusters of Ca and Nd and their effects on the Cottrell atmosphere are attributed to several factors. The results of the present study indicate that the content of the Ca and Nd solutes are one of the main factors influencing the Cottrell atmosphere caused by the solute clusters. It may also be considered to analyze the factors attributable to differences in other external parameters of Ca and Nd. The process of comparing and analyzing the properties of each alloy by varying the content of Ca and Nd solute is required. It is also worth noting the intrinsic difference between Ca and Nd elements. It includes, for example, the effects of atomic radius ($R_{Nd} < R_{Ca}$) and diffusivity ($D_{Nd} < D_{Ca}$) [41] and their interactions with clusters and dislocations. Ca has a larger atomic radius and higher diffusivity compared to Mg and Mn. On the other hand, the atomic radius and diffusivity of Nd are very similar to that of Mg, unlike Ca. The potential for these differences to affect solute cluster formation and impede dislocation movement can be discussed. The process of identifying it should be accompanied by various data mining procedures for a number of APT tips based on the varying content of Ca and Nd alloys.

5. Conclusion

In this study, the microstructure and the mechanical properties under various temperatures and strain rates of the extruded Mg-Mn, Mg-Mn-Ca, and Mg-Mn-Nd alloys were analyzed to investigate the effect of Ca and Nd on plastic instability in Mg-Mn alloy. The main results of the present study are summarized below.

(1) The PLC effect showed a clear difference depending on alloying elements, temperature, and strain rate. The most pronounced PLC phenomenon was observed in MN11 alloy under deformation at an elevated temperature (100 to 200 °C) and at a low strain rate (10^{-4} to 10^{-3} /s) in tested conditions
(2) The low fraction of Ca in the matrix of MX10 alloy causes the formation of low number density Mn-Ca and Ca-Ca solute clusters and an unbalanced Mn:Ca ratio, thereby reducing the PLC effect.
(3) In Mg-Mn-based alloys with a weakened texture, the deterioration of mechanical properties is clearly observed in a certain range of deformation conditions despite being de-

formed at elevated temperatures, which is closely related to the occurrence of plastic instability.

Declaration of Competing Interest

The authors declare that they have no known competing financial interests or personal relationships that could have appeared to influence the work reported in this paper.

Acknowledgement

The authors are grateful for the financial support of German Research Foundation (DFG) (Grant Nr. YI103/3-1 and AL1343/8-1).

References

[1] A. Yilmaz, Sci Technol Adv Mater 12 (2011) 063001.
[2] H. Ovri, E.T. Lilleodden, Acta Mater 89 (2015) 88–97.
[3] C.Q. Li, D.K. Xu, B.J. Wang, L.Y. Sheng, E.H. Han, J Mater Sci Technol 32 (2016) 1232–1238.
[4] C. Corby, C.H. Cáceres, P. Lukáč, Mater Sci Eng: A 387-389 (2004) 22–24.
[5] H. Ovri, D. Steglich, H. Dieringa, E.T. Lilleodden, Mater Sci Eng: A 740-741 (2019) 226–234.
[6] M. Pozuelo, Y.W. Chang, J. Marian, J.M. Yang, Scr Mater 127 (2017) 178–181.
[7] N. Stanford, I. Sabirov, G. Sha, A. La Fontaine, S.P. Ringer, M.R. Barnett, Metall Mater Trans A 41 (2010) 734–743.
[8] L. Jiang, J.J. Jonas, R. Mishra, Mater Sci Eng: A 528 (2011) 6596–6605.
[9] J. Min, L.G. Hector, J. Lin, J.T. Carter, A.K. Sachdev, Int J Plast 57 (2014) 52–76.
[10] T. Wang, J.J. Jonas, H. Qin, S. Yue, Mater Sci Eng: A 645 (2015) 126–135.
[11] W.H. Wang, D. Wu, S.S. Shah, J.H. Ni, R.S. Chen, X.N. Zhang, Philos Mag Lett 97 (2017) 235–240.
[12] W.H. Wang, D. Wu, R.S. Chen, X.N. Zhang, J Mater Sci Technol 34 (2018) 1236–1242.
[13] D. Wu, R.S. Chen, E.H. Han, Mater Sci Eng: A 532 (2012) 267–274.
[14] C.Q. Li, D.K. Xu, T.T. Zu, E.H. Han, L. Wang, J Magnesium Alloys 3 (2015) 106–111.
[15] T.Q. Li, Y.B. Liu, Z.Y. Cao, R.Z. Wu, M.L. Zhang, L.R. Cheng, D.M. Jiang, J Alloys Compd 509 (2011) 7607–7610.
[16] C. Wang, Y.B. Xu, E.H. Han, J Metall 2012 (2012) 1–5.
[17] S.K. Wu, C. Chien, C.S. Yang, H.Y. Bor, Mater Sci Eng: A 605 (2014) 33–38.
[18] T. Wang, L. Jiang, R.K. Mishra, J.J. Jonas, Metall Mater Trans A 45 (2014) 4698–4709.
[19] M. Chaturvedi, D.J. Lloyd, K. Tangri, Metal Sci J 6 (2013) 16–19.
[20] T. Al-Samman, X. Li, Mater Sci Eng: A 528 (2011) 3809–3822.
[21] I. Basu, T. Al-Samman, Acta Mater 67 (2014) 116–133.
[22] J. Bohlen, M.R. Nürnberg, J.W. Senn, D. Letzig, S.R. Agnew, Acta Mater 55 (2007) 2101–2112.
[23] J. Bohlen, J. Wendt, M. Nienaber, K.U. Kainer, L. Stutz, D. Letzig, Mater Charact 101 (2015) 144–152.
[24] D.W. Kim, B.C. Suh, M.S. Shim, J.H. Bae, D.H. Kim, N.J. Kim, Metall Mater Trans A 44 (2013) 2950–2961.
[25] Z.R. Zeng, Y.M. Zhu, S.W. Xu, M.Z. Bian, C.H.J. Davies, N. Birbilis, J.F. Nie, Acta Mater 105 (2016) 479–494.
[26] J. Bohlen, S. Yi, D. Letzig, K.U. Kainer, Mater Sci Eng: A 527 (2010) 7092–7098.
[27] P. Hidalgo-Manrique, V. Herrera-Solaz, J. Segurado, J. Llorca, F. Gálvez, O.A. Ruano, S.B. Yi, M.T. Pérez-Prado, Acta Mater 92 (2015) 265–277.
[28] P. Hidalgo-Manrique, S.B. Yi, J. Bohlen, D. Letzig, M.T. Pérez-Prado, Metall Mater Trans A 44 (2013) 4819–4829.
[29] S.K. Woo, R.S. Pei, T. Al-Samman, D. Letzig, S.B. Yi, J Magnesium Alloys 10 (2022) 146–159.
[30] R. Pei, S.K. Woo, S. Yi, T. Al-Samman, Mater Sci Eng: A 835 (2022).
[31] G. Ananthakrishna, Phys Rep 440 (2007) 113–259.
[32] K. Chihab, Y. Estrin, L.P. Kubin, J. Vergnol, Scripta Metall Mater 21 (1987) 203–208.
[33] W.H. Wang, D. Wu, S.S.A. Shah, R.S. Chen, C.S. Lou, Mater Sci Eng: A 649 (2016) 214–221.
[34] A. Chapuis, Q. Liu, Int J Solids Struct 152-153 (2018) 217–227.
[35] R.C. Picu, Acta Mater 52 (2004) 3447–3458.
[36] E. Rizzi, P. Hähner, Int J Plast 20 (2004) 121–165.
[37] S. Dhara, R.K.W. Marceau, K. Wood, T. Dorin, I.B. Timokhina, P.D. Hodgson, Data Brief 18 (2018) 968–982.
[38] S. Zhu, H.-.C. Shih, X. Cui, C.-.Y. Yu, S.P. Ringer, Acta Mater (2021) 203.
[39] S.M. Zhu, J.F. Nie, Scr Mater 50 (2004) 51–55.
[40] A.H. Cottrell, B.A. Bilby, Proc Phys Soc Lond Sect A 62 (1949) 49–62.
[41] B.-.C. Zhou, S.-.L. Shang, Y. Wang, Z.-.K. Liu, Acta Mater 103 (2016) 573–586.